Time-Resolved Structural Kinetics of an Organic Mixed Ionic Electronic Conductor

*Bryan D. Paulsen, Ruiheng Wu, Christopher J. Takacs, Hans-Georg Steinrück, Joseph Strzalka, Qingteng Zhang, Michael F. Toney, Jonathan Rivnay**

Dr. B. D. Paulsen, R. Wu, Prof. J. Rivnay
Department of Biomedical Engineering, Northwestern University, Evanston, IL 60208, USA
E-mail: jrivnay@northwestern.edu

Dr. C. J. Takacs, Dr. M. F. Toney[#]
Stanford Synchrotron Radiation Lightsource, SLAC National Accelerator Laboratory, Menlo Park, CA 94025, USA
[#]Present address: Department of Chemical and Biological Engineering, University of Colorado, Boulder, CO 80309, USA

Prof. Hans-Georg Steinrück
Department Chemie, Universität Paderborn, Warburger Str. 100, 33098 Paderborn, Germany

Dr. J. Strzalka, Dr. Q. Zhang
X-Ray Science Division, Argonne National Laboratory, Lemont, Illinois 60439, USA

Keywords: operando, in situ, GIWAXS, OMIECs, PEDOT:PSS

The structure and packing of organic mixed ionic-electronic conductors have an outsized effect on transport properties. In operating devices this structure is not fixed but is responsive to changes in electrochemical potential, ion intercalation, and solvent swelling. Towards this end, the steady state and transient structure of the model organic mixed conductor, poly(3,4-ethylenedioxythiophene) polystyrene sulfonate (PEDOT:PSS), is characterized using multimodal time-resolved operando techniques. Steady state operando X-ray scattering reveals a doping induced lamellar expansion of 1.6 Å followed by 0.4 Å relaxation at high doping levels. Time-resolved operando X-ray scattering reveals asymmetric rates of lamellar structural change during doping and dedoping that do not directly depend on potential or charging transients. Time-resolved spectroscopy establishes a link between structural transients and the complex kinetics of electronic charge carrier subpopulations, in particular the polaron-bipolaron equilibrium. These findings provide insight into the factors limiting the response time of organic mixed conductor based devices, and present the first real-time

observation of the structural changes during doping and dedoping of a conjugated polymer system via X-ray scattering.

Organic mixed ionic-electronic conductors (OMIECs) are a class of conjugated materials[1] of growing interest for bioelectronic,[2] energy storage,[3] electrochromic,[4] and neuromorphic computing[5] applications due to their ability to simultaneously transport both ionic and electronic charge, and couple between the two. Across applications, many OMIEC-based devices under operating conditions undergo changes in structure and system composition due to the uptake and expulsion of ions and solvent, and the modulation of electronic charge on the conjugated OMIEC backbone.[6–8] This greatly complicates the establishment of predictive structure-property relationships with which to guide the design of next generation OMIECs, as static (often dry) structure is no longer sufficient for drawing these relationships. This has motivated the investigation of OMIECs and related materials with ex situ, in situ, and operando methods. Grazing incidence wide angle X-ray scattering (GIWAXS) has been widely employed to investigate conjugated materials, as the probed crystalline fraction, texture, and/or order generally dictate ultimate charge transport properties.[9,10] Previously, GIWAXS has been carried out on ex situ electrochemically doped conjugated polymers[11] and OMIECs[7] to quantify their electrochemical potential dependent structural changes, generally manifesting as a π-stack spacing contraction and lamellar spacing expansion upon electrochemical doping. Ex situ methods intrinsically limit structural characterization to dry steady state conditions, and in the case of volatile solvents do not capture the contributions of solvent swelling. In situ and operando grazing incidence[12] and transmission[13] X-ray scattering methods have allowed for quantification of the electrochemical doping dependent steady state structure of conjugated polymers in contact with electrolytes under applied potentials. Nevertheless, thus far these methods could not be extended to time-resolved measurements to understand transient structural behavior far from steady state. For instance,

the structure of a polythiophene in contact with a polymerized ionic liquid electrolyte measured with operando GIWAXS has been reported,[12] however the very slow response of the polymerized ionic liquid electrolyte prevent the investigation of any transient structural behavior of the conjugated polymer. For OMIEC applications the transient structure is of equal if not greater importance than the steady-state structure.

Taking inspiration from the time-resolved GIWAXS investigation of conjugated polymers and OMIECs carried out during film formation and drying,[14,15] we have carried out operando time-resolved GIWAXS of the prototypical OMIEC, PEDOT:PSS, during step potential transients, and in the more common steady-state potential regime. A variety of techniques have been employed to produce high electrical conductivity PEDOT:PSS films.[16] One of the most effective methods to maximize electronic properties is crystallization via the exposure to sulfuric acid,[17] which has been shown to produce high performance and high stability organic electrochemical transistors for bioelectronic applications.[18] Acid crystallized PEDOT:PSS has the added benefit of producing reasonably ordered, well-textured films exhibiting high scattering intensities, making it an ideal candidate for in situ and operando GIWAXS measurements. Steady-state in situ structural characterization mapped the potential dependent scattering intensity and lattice spacings. Transient operando multi-modal structural and spectroscopic characterization revealed complex structural transients that unexpectedly diverged from simple charge or potential transients, but instead followed the polaron-bipolaron population kinetics. These results have significant implications for the future design of OMIECs, especially in applications that require fast response times.

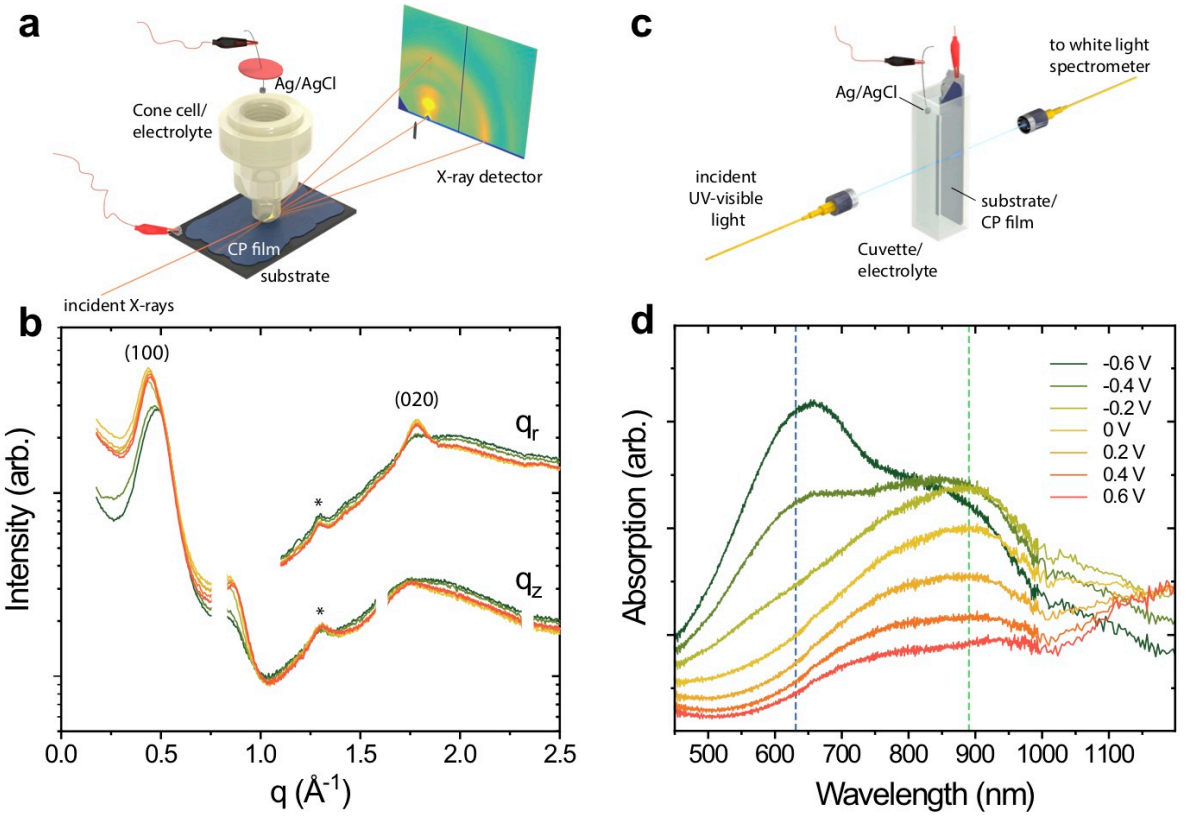

Figure 1. Operando scattering and spectroscopy of acid-crystallized PEDOT:PSS. Diagram of the (a) electrochemical cell with operando GIWAXS. (b) Nominally out-of-plane (q_z) and in-plane (q_r) line-cuts (q_r > 1.0 Å^{-1}) taken from 2-D scattering plots of PEDOT:PSS films in the operando cell under applied potential (same legend as in (d)) highlighting the in-plane π-stack (020) and out-of-plane lamellar (100) scattering. Asterisks (*) denote parasitic scattering from PEEK cone cell. Diagram of the (c) UV-vis-NIR spectroelectrochemical cell. (d) UV-Vis-NIR spectra under various applied potentials highlighting the changes in the neutral π-π* and charged polaronic absorptions centered around 630 nm (blue dashed line) and 890 nm (green dashed line), respectively.

Static 2-D GIWAXS patterns of drop-cast acid crystallized PEDOT:PSS were measured (Figure S1a) revealing a structure consistent with previously reported literature.[17–20] On the whole, the strong texturing and previously inferred high degree of crystallinity of acid crystallized PEDOT:PSS[17,18] yield strong anisotropic scattering that makes it attractive for

operando electrochemical experiments, allowing for shorter exposure times at the same incident flux, and the potential to overcome strong background scattering from the electrolyte and cell material. These attributes, combined with precise control of beam height and footprint, were necessary for successful operando scattering measurements.

The operando semicrystalline structure during electrochemical measurements was directly probed with GIWAXS using a machined polyether ether ketone (PEEK) cone cell that contacted the sample substrate defining the area of film exposed to electrolyte (~0.20 cm^2), **Figure 1a**. This cell is based on that developed for precision electrochemistry for electrochemical energy storage and is readily adopted for the present study.[21–24] The PEEK wall thickness (1.5 mm) machined down to a knife edge was sufficiently thin that the attenuation of the scattered intensity was not prohibitive (Figure S1b). Due to the machined knife edge, attenuation of the low angle incident beam was minimal, scattered intensity was increasingly attenuated with increasing scattering angle, reaching ~50% attenuation at 25°, due to a PEEK pathlength of ~1.1 mm. The film thickness (~3-6 μm) and vertically focused beam height (< 10 μm) were necessary to minimize the electrolyte background scattering, allowing the resolution of the in-plane π-stack and out-of-plane lamellar scattering from acid crystallized PEDOT:PSS immersed in aqueous electrolyte under applied electrochemical potential. 2-D GIWAXS patterns collected with the acid crystallized PEDOT:PSS inside the PEEK electrochemical cell filled with 100 mM aqueous NaCl retain the edge-on oriented structure, and despite the large electrolyte scattering background, the in-plane π-stack and out-of-plane lamellar scattering peaks are still resolvable (**Figures 1b**). System stability was high, as over the course of all operando studies, beam damage was not apparent and minimal peaks shifts were observed, (Figure S1b-f, Table S1).

In parallel to the operando GIWAXS measurements, electrochemistry with operando UV-vis-NIR transmission spectroscopy (spectroelectrochemistry) was carried out to probe the neutral and charged (polaron and bipolaron) states during electrochemical measurements (**Figure 1c**). Spectra from 400 to 1200 nm under applied electrochemical potential (**Figure 1d**) displayed a neutral π-π* absorption centered around 630 nm, a polaronic absorption centered around 890 nm, and the onset of a bipolaronic absorption beginning above 1000 nm and centered at a higher wavelength beyond the instrument range.[25–28] These spectroelectrochemical measurements allowed the direct assessment of the relative neutral and polaron populations from the resolved neutral and polaron absorptions, and by inference the relative bipolaron population.

Electrochemically cycling the film (*i.e.* cyclic voltammetry) while simultaneously collecting 2-D GIWAXS patterns or UV-vis-NIR spectra allowed the real-time tracking of potential dependent lamellar and π-scattering behavior, along with relative neutral and polaron populations (**Figure 2**). The potential was swept at 5 mV/s to allow a longer X-ray detector integration time of 10 s for better peak resolution. The voltage and current density traces over time (**Figure 2a,b**) reflected a PEDOT:PSS film charging and discharging in a capacitive manner with relatively flat current plateaus.[29,30] The potential range was limited to ±0.6 V vs Ag/AgCl, as the applied voltages were low enough to avoid electrolyte breakdown yet large enough to probe the range of reproducible scattering peak shifts. Plotted as current density versus potential (Figure S2a), the cyclic voltammograms display a capacitive hysteresis common to PEDOT:PSS films cycled over similar potential ranges.[31] The out-of-plane lamellar scattering peak displayed the largest change during cycling, shifting to higher q_z toward the negative extreme (E < 0 V vs Ag/AgCl) of the dedoping (reduction) sweep, returning to lower q_z during initial doping (oxidation) sweep, reaching a minimum q_z around 0 V vs Ag/AgCl), and relaxing to a slightly higher q_z toward the positive extreme (E > 0 V vs

Ag/AgCl) of the doping (oxidation) sweep, as shown in the line-cut color-map in **Figure 2c**. This pattern of q_z lamellar peak shift proved to be reversible, repeating itself upon successive voltage sweeps (Figure S2b). Interestingly, the π-stack scattering does not show a significant shift in q_r position from the strong underlying background, but instead was dramatically diminished in intensity upon reductive dedoping (E > 0 V vs Ag/AgCl), with a simultaneous increase in the scattering background at larger q_r, (Figure S3b). As with the lamellar peak shifts, the changes in the π-stack scattering proved to be reversible, repeating itself upon successive potential cycling.

The increased high-q electrolyte scattering background during reductive dedoping (E > 0 V vs Ag/AgCl) was accompanied by a decrease in the low-q scattering background and lamellar scattering intensity. The uptake of cations and water upon dedoping disrupted the packing of the PEDOT:PSS, broadening the (100) peak by about 35%. After accounting for the experimental resolution,[32] calculating the mean number of Bragg planes contributing to the scattering, $\overline{N}_{100} = q_{100}/\Delta q_{100}$, showed a reduction from 3.9 to 3.0. Correspondingly, the intensity of the 100 peak, which is proportional to the square of the number of scatterers,[33] for the dedoped state dropped to about 60% ($3.0^2/3.9^2$) of the intensity observed for the doped state. In addition to the decrease in lamellar scattering, the low-q scattering background at -0.6 V vs Ag/AgCl decreased ~65% relative to the doped state. The changes in low-q scattering background are ascribed to changes in film thickness,[34] composition, and meso-scale structure that coincide with potential dependent swelling, and are the focus of future study.

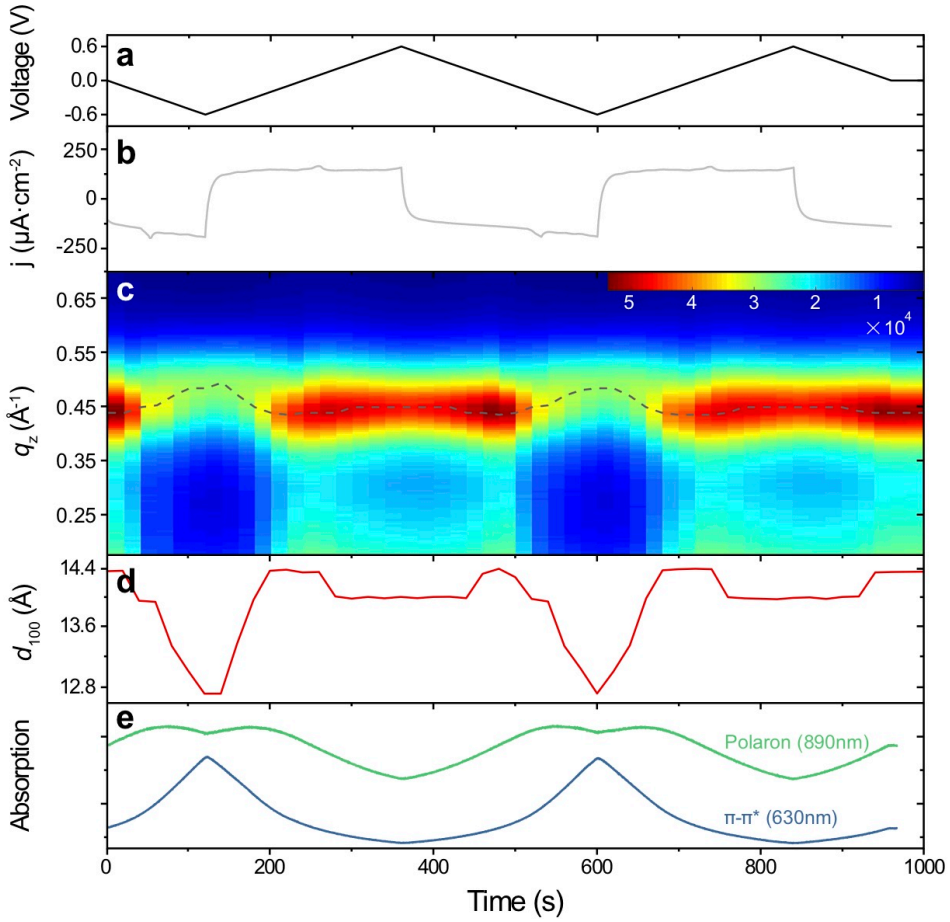

Figure 2. Cycled linear potential sweeps during operando GIWAXS and UV-vis-NIR spectroscopy: (a) Potential profile, (b) current density traces, (c) out-of-plane scattering intensity color map, (d) lamellar d-spacing, and (e) 630 nm π-π* (blue line) and 890 nm polaronic (green line) absorption over time. The dotted line in (d) serves to indicate the maximum lamellar scattering intensity at each time step.

The position of the lamellar scattering was fit to calculate the average d_{100} lamellar spacing plotted over time in **Figure 2d**. The potential-dependent scattering behavior implies a contracted lamellar d-spacing of 13.0 Å and relatively disordered π-stack in the (relatively) dedoped state (E < 0 V vs Ag/AgCl). When doped (E ~ 0 V vs Ag/AgCl) the lamellar d-spacing expands to 14.3 Å and the π-stack becomes quite ordered with a d-spacing of 3.53 Å. This is roughly analogous to the often reported π-stack contraction and lamellar expansion seen in electrochemically or molecularly doped polyalkylthiophenes.[11–13,35,36] Though in this

case, any change in π-stack d-spacing was overshadowed by changes in π-stack scattering intensity. However, with further doping (E > 0 V vs Ag/AgCl) while the π-stack maintains it degree of order and d-spacing, the lamellar d-spacing relaxes to 14.05 Å. Analogous cyclic spectroelectrochemical experiments revealed the polaron and π-π* absorption to roughly track the structural evolution (**Figure 2e**), but with a local polaron minimum and π-π* maximum coinciding with the dedoped d_{100} contraction minimum, and a global polaron minimum and π-π* minimum coinciding with the highly doped d_{100} relaxation. The polaron absorption reached its maximum around -0.2V vs Ag/AgCl, but was symmetric with potential sweep direction, unlike the d_{100} which shows hysteretic behavior about -0.2V vs Ag/AgCl.

Whereas, in polyalkylthiophenes, further doping is likely to drive dopant anions into the sidechain lamellae, thus further expanding the lamellae spacing with increasing degree of doping,[8,11,12] here the dopant anion is tethered to the PSS chains already present between PEDOT layers, thus increasing the degree of doping occurs by depleting the PSS chains of some of their charge balancing cations. Specifically, the further doping of PEDOT:PSS requires the loss of material (cations and their solvating water molecules) from between the PEDOT layers, resulting in a decrease in the lamellar d-spacing.

From comparing the real-time potential cycled GIWAXS data with GIWAXS patterns collected after equilibrating at a fixed potential, the potential sweep rate (5mV/s) was sufficiently slow as to closely approximate the equilibrated/steady-state potential dependent structure, Figure S3. The equilibrated constant potential GIWAXS data showed the same potential dependent d-spacing and scattering intensity behavior for E < 0 V vs Ag/AgCl, confirming the d_{100} hysteresis around -0.2 V vs Ag/AgCl. However, for E > 0 V vs Ag/AgCl, the equilibrated measurements showed the relaxed d_{100} to have a slight potential dependence,

with d_{100} slightly decreasing (the (100) peak shifting to higher q_z, Figure S3a) with increasing positive voltage, indicating that this lamellar relaxation occurs over long time scales.

From cyclic linear sweep spectroelectrochemistry, the neutral π-π* absorption centered about 630 nm was found to be strongest in the dedoped state under a reductive potential of -0.6 V vs Ag/AgCl, and was successively bleached with application of more positive potential, (Figure 2e). This was to be expected as the high degree of doping and charge delocalization were expected to consume all the neutral species (thiophene rings) in the film. The polaron absorption centered about 630 nm was found to be strongest under potentials between -0.3 to -0.4 V vs Ag/AgCl. At potentials more positive than -0.3 V vs Ag/AgCl the polaron absorption diminished. This implies the increasingly preferential formation of bipolaronic charge species with further oxidative potential. Likewise, for potentials more negative than -0.4 V vs Ag/AgCl the polaron absorption diminished, as electronic charge was removed from the film and the polaronic species were converted back to neutral.

Under operating conditions, OMIECs present responsive systems that are not necessarily at equilibrium. Therefore, time-resolved GIWAXS was carried out during potential step and subsequent holding to track the transient structural evolution. Chronoamperometry was carried out by recording the current during potential steps to and from 0 and ±0.6 V vs Ag/AgCl, during continuous 0.5 s GIWAXS exposures (**Figure 3a & b**). While signal to noise limitations prohibited adequate resolution of the in-plane π-stack peak during 0.5 s exposures, the lamellar scattering feature was still sufficiently resolved as to allow tracking of the structural transients. The color map of the q_z line cuts shows the evolution of the (100) peak position transients following potential steps (**Figure 3c**). Converting peak position to d-spacing, the largest change in d_{100} (~1.5 Å) occurred when stepping the potential to and from 0 and -0.6 V vs Ag/AgCl, representing dedoping (0 to -0.6V) and redoping (-0.6 to 0 V) of the

film (**Figure 3d**). Further modulation of the doping with potential steps to and from 0 and +0.6 V vs Ag/AgCl produced a moderate lamellar contraction from 14.3 to 14.05 Å.

The time scales of the lamellar d-spacing changes accompanying the dedoping (0 to -0.6 V) and doping (-0.6 and 0 V) steps were not symmetric, with the d_{100} contraction during dedoping occurring faster than the d_{100} expansion during doping. Empirically fitting the d_{100} transients revealed the time constant during doping ($\tau_{d,-0.6\rightarrow 0V} = 0.72 \pm 0.06$ s) to be over twice that during dedoping ($\tau_{d,0\rightarrow -0.6V} = 0.32 \pm 0.17$ s) (see equation S1). Moreover, during the slower process of doping the lamellar d_{100} initially expanded to 14.4 Å, which was effectively (>95%) complete in 4 s. However, that represented an overshoot, which after 10 s began to slowly relax to its equilibrated value of 14.3 Å, (see from 50 to 60 s and from 130 to 140 s in **Figure 3d**). This is in contrast to the dedoping d_{100} contraction to 12.9 Å, which was effectively (>95%) complete in under 2 s and did not overshoot.

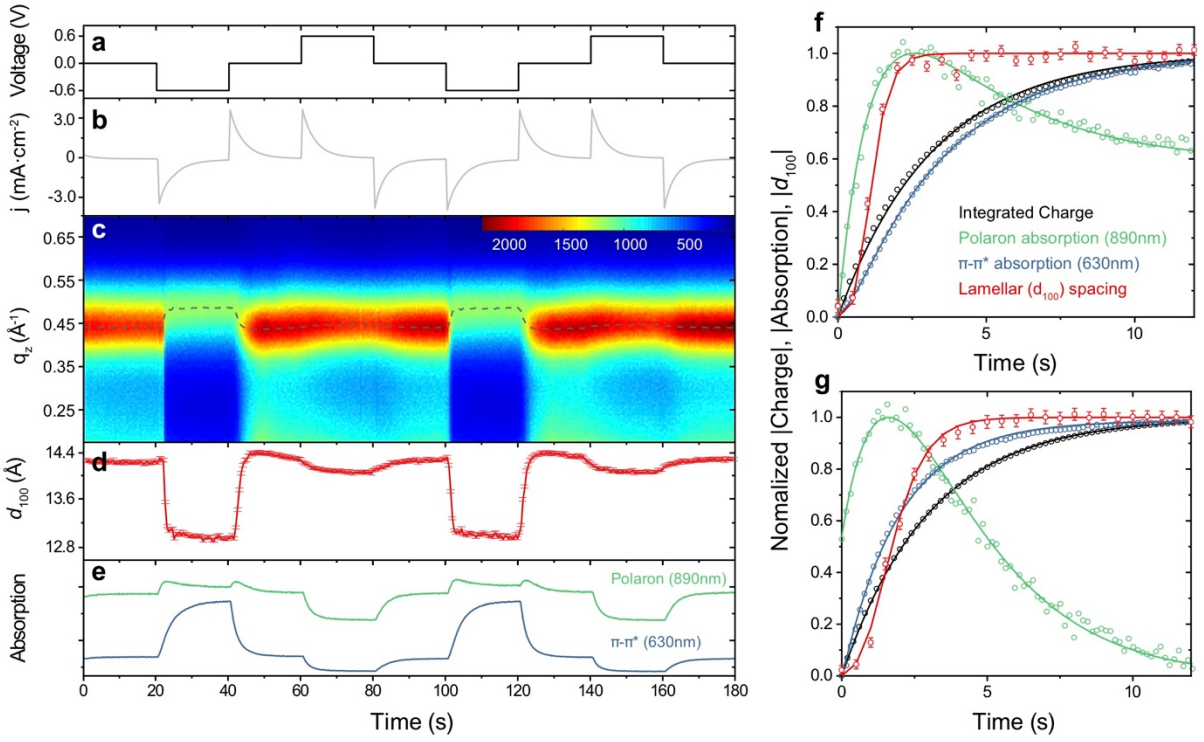

Figure 3. Potential step with time-resolved operando GIWAXS and UV-vis-NIR spectroscopy: (a) Potential profile, (b) charging current density traces, (c) out-of-plane

scattering intensity color map, (d) lamellar d-spacing, and (e) 630 nm π-π* (blue line) and 890 nm polaronic (green line) absorption over time. The dotted line in (d) serves to indicate the maximum lamellar scattering intensity at each time step. Normalized changes in integrated charge, 890 nm polaronic absorption, 630 nm π-π* absorption, and d_{100} over time during (f) dedoping (0 to -0.6 V vs Ag/AgCl) and (g) doping (0 to -0.6 V vs Ag/AgCl) transients. For figure (f) and (g), open circles represent the experimental data and solid lines represent the model fits. Error bars for d-spacings in (d), (f), and (g) reflect the 99.7% confidence interval (±3 standard deviations) of the peak fits from the centers of which the d-spacing was calculated, instrument error in the current (charge) and absorption data were negligible.

The forward and reverse potential steps from 0 and +0.6 V vs Ag/AgCl produced much slower and more symmetric d_{100} transients, with both processes following roughly equivalent time constants ($\tau_{d,0\rightarrow-0.6V}$ = 2.25 ± 0.76 s, $\tau_{d,+0.6\rightarrow0V}$ = 2.56 ± 0.50 s) that were over seven times slower than the fast dedoping process. The overall transient behavior was not unique to the lamellar spacing but was mirrored by the transient behavior of the π-stack scattering intensity, and low and high q scattering background, strongly implying that the potential dependent structural transformations occurs synchronously.

The simultaneously collected chronocoulometric data was readily fit with a simple RC model. The charging time constants for potentials steps between 0 and -0.6 V vs Ag/AgCl ($\tau_{q,-0.6\rightarrow0V}$ = 3.69 ± 0.74 s, $\tau_{q,0\rightarrow-0.6V}$ = 3.34 ± 0.72 s) (Figure 3f) and between 0 and +0.6 V vs Ag/AgCl ($\tau_{q,+0.6\rightarrow0V}$ = 3.58 ± 0.54 s, $\tau_{q,0\rightarrow+0.6V}$ = 3.34 ± 0.72 s) where all quite similar. On the whole, the structural transients outpaced the electrochemical charging of the films (**Table 1**), showing that complete charging of the film was not the rate limiting process dictating the rate of

structural change. Nor did the structural transients align with the expected potential transients in the PEDOT:PSS film, assuming RC behavior.

Table 1. Time and rate constants for charge, d-spacing, and absorption kinetics

ΔE [V vs Ag/AgCl]	$\tau_{q,GIWAXS}$ [s]	τ_{d100} [s]	$\tau_{q,UV\text{-}vis}$ [s]	$k_{n\rightarrow p}$ [s^{-1}]	$k_{p\rightarrow n}$ [s^{-1}]	$k_{p\rightarrow bp}$ [s^{-1}]	$k_{bp\rightarrow p}$ [s^{-1}]
0 → -0.6	3.34 ± 0.72	**0.32 ± 0.17**	3.35 ± 0.40	--	0.26 ± 0.08[b]	--	**0.93 ± 0.15**[c]
-0.6 → 0	3.69 ± 0.74	**0.72 ± 0.06**	3.00 ± 0.01	0.50 ± 0.01[a]	--	**0.42 ± 0.02**[c]	--
0 → +0.6	3.34 ± 0.72	2.25 ± 0.76	3.00 ± 0.22	0.54 ± 0.04[a]	--	0.48 ± 0.01[c]	--
+0.6 → 0	3.58 ± 0.54	2.56 ± 0.50	2.58 ± 0.03	--	0.29 ± 0.01[a]	--	0.34 ± 0.01[c]

[a]Extracted from π-π* absorption transients; [b]extracted from π-π* and polaron absorption transients; [c]extracted from polaron absorption transients. 95% confidence intervals were calculated for the fit constants. Time and rate constants listed were averaged across equivalent potential steps. The error listed above is the larger of either the 95% confidence interval of the fit parameters or two standard deviations of the distribution average. The asymmetric structural time constants and their related limiting kinetic constants are in bold.

In order to further probe this lack of correlation between structural and electrochemical transients, analogous transient spectroelectrochemical experiments were carried out. Operando transmission UV-vis-NIR spectra were collected during transient potential steps (**Figure 3e**). While the optical absorption data correlated with total charge, it also gave insight into the relative populations of neutral states, singly charged polarons, and dually charged bipolarons on the PEDOT backbone.

The absorption kinetics were modelled as two consecutive elementary reactions:

$$n \underset{k_{p\rightarrow n}}{\overset{k_{n\rightarrow p}}{\rightleftharpoons}} p + e^- \underset{k_{bp\rightarrow p}}{\overset{k_{p\rightarrow bp}}{\rightleftharpoons}} bp + e^- \quad (1)$$

where equilibrium population of neutral (*n*), polaronic (*p*), and bipolaronic (*bp*) species was determined by the electrochemical potential, and the polaron population was an intermediary between the neutral and bipolaronic species. The concentrations of *n* and *p* were directly proportional to the 630 and 890 nm absorptions, respectively, and from their transient

response the forward and reverse rate constants for both elementary reactions were calculated (see Equation S3 through S7).

The neutral-polaron kinetic parameters extracted from both π-π* and polaronic absorption transients were consistent across all potential step measurements, with the average neutral-to-polaron rate constant ($k_{n\rightarrow p}$ = 0.521 ± 0.047 s^{-1}) being twice the average of the reverse polaron-to-neutral rate constant ($k_{p\rightarrow n}$ = 0.269 ± 0.066 s^{-1}). Likewise, the polaron-to-bipolaron rate constants as determined from the polaron bleach kinetics were consistent giving an average value of $k_{p\rightarrow bp}$ = 0.451 ± 0.075 s^{-1}. However, the extracted bipolaron-to-polaron rate constants varied significantly. During the 0 and -0.6 V vs Ag/AgCl dedoping potential step, the bipolaron-to-polaron kinetics were fast, with $k_{bp\rightarrow p}$ = 0.93 ± 0.15 s^{-1} and >1 s^{-1} as determined from the bleach of the polaron absorption and the growth of the neutral absorption, respectively. Conversely, modulating the degree of doping by stepping the potential from +0.6 and 0 V vs Ag/AgCl, resulted in much slower bipolaron-to-polaron conversion, with an extracted rate constant of only $k_{bp\rightarrow p}$ = 0.337 ± 0.005 s^{-1}.

It is possible that the structural kinetics would follow one or both of the charged population kinetics (p and/or bp). However, the polaron-to-neutral kinetics does not clarify the structural kinetics, as the asymmetric rapid lamellar contraction during dedoping (0 to -0.6 V vs Ag/AgCl) and slower expansion during doping (-0.6 to 0 V vs Ag/AgCl) is the inverse of the slower polaron-to-neutral kinetics during dedoping and faster neutral-to-polaron kinetics during doping (**Figure 3f,g**). Nor can the lamellar spacing depend on the total polaron concentration, as shown above (Figure 2d,e), the polaron absorption does not show any hysteresis about -0.2 V vs Ag/AgCl, whereas the lamellar spacing does (Figure S2b). Further, the initial transient increases in polaron concentration upon both 0 to -0.6 and -0.6 to 0 V vs

Ag/AgCl potential steps (Figure 3e) should *both* be (but are not) accompanied by similar d_{100} contractions (Figure 3d). Instead, the asymmetric structural kinetics correlate with the variable bipolaron-to-polaron rates.

The rapid depletion of bipolaronic species and production of polaronic species during dedoping (0 to -0.6 V vs Ag/AgCl) is followed in quick succession by a similarly rapid d_{100} contraction, as seen in the initial rise in polaronic absorption and change in d_{100} (Figure 3f). By the time polaronic absorption begins to fall, due to the rate of conversion of polaronic species to neutral species overtakes the rate of production of polaronic species from bipolaronic species, the d_{100} has equilibrated. Both the π-π* absorption and the total integrated charge lag considerably behind the d_{100} change. Conversely during doping (-0.6 to 0 V vs Ag/AgCl), d_{100} is slow change until the polaronic absorption begins to fall, this time due to the rate of conversion of polaronic species from neutral species being overtaken by the rate of production of polaronic species from bipolaronic species, at which point d_{100} then equilibrates (**Figure 3g**). Again, both the π-π* absorption and the total integrated charge lag considerably behind the d_{100} change. In both cases the d_{100} change clearly follows the conversion between polaronic and bipolaronic species. Likewise, the slower d_{100} expansion when stepping from -0.6 to 0 V vs Ag/AgCl and relaxation when stepping between 0 and +0.6 V vs Ag/AgCl seems to follow the slower polaron-bipolaron kinetics during those potential steps.

While the polaron-bipolaron kinetics dictate the d_{100} kinetics, the physical explanation for the forward and reverse difference of these kinetics is not directly obvious. Often asymmetric or hysteretic behavior is attributed to electronic charge trapping. If significant electronic charge were trapped in the film, one would expect a delay in the extraction of charge during dedoping potential steps. However, here the charge extraction and injection during dedoping and doping potential steps was essentially identical (Figure 3 f-g and Table 1), making it

unlikely that charge trapping was the source of the asymmetric structural and polaron-bipolaron kinetics.

Our simple kinetic model presumes that the only reaction pathway between polaronic and bipolaronic species is the addition or removal of an electron. It is also possible that two polarons can combine to form a bipolaron, or the reverse, a bipolaron may split into two polarons.

$$p + p \underset{k'_{bp\rightarrow p}}{\overset{k'_{p\rightarrow bp}}{\rightleftharpoons}} bp \quad (2)$$

This reaction pathway may play a significant role when the system is stepped far from its doped equilibrium during the 0 to -0.6 V vs Ag/AgCl dedoping step, thus leading to the perceived increase in the bipolaron-to-polaron rate constant.

While the admittedly simplistic kinetic model accounts for the absorption transients observed here, the potential dependent charge carrier populations are likely more complicated, including multi polaronic and bipolaronic species in addition to simple polarons and bipolarons.[28] While this complicates the charge carrier classification, the absorption kinetics remain the same, with the kinetics of the absorption centered around 890 nm still seemingly linked to the d_{100} kinetics.

In conclusion, we have for the first time measured the time resolved structural evolution of a conjugated polymer during electrochemical doping and dedoping via operando GIWAXS. Compared to the steady-state in situ measurements, the time-resolved operando GIWAXS revealed asymmetric rates of structural change. Operando spectroscopy revealed that the transient structural behavior is tied to the complex transient polaron-bipolaron kinetics, as the structure depends on the nature of the charge carriers present on the polymer backbone (i.e.

whether polaronic or bipolaronic). Since the presence of charge carriers as polarons and bipolarons is not unique to PEDOT:PSS, but common to conjugated polymers, it is likely that this is a generalizable phenomenon. This is an interesting result, as much of the work to improve OMIEC device time response has focused on improving ion transport[37] and reducing device dimensions.[38,39] This work shows that even in such optimized settings bipolaron population kinetics likely present a limit to device speed. This begs the question, can OMIECs be designed to tailor electronic charge carrier population kinetics? As of now, this is an unexplored area of research.

Supporting Information
Supporting Information is available from the Wiley Online Library or from the author.

Acknowledgements
B.P., R.W., and J.R. gratefully acknowledge support from the National Science Foundation Grant No. NSF DMR-1751308. This research used resources of the Advanced Photon Source, a U.S. Department of Energy (DOE) Office of Science User Facility operated for the DOE Office of Science by Argonne National Laboratory under Contract No. DE-AC02-06CH11357. Use of the Stanford Synchrotron Radiation Lightsource, SLAC National Accelerator Laboratory, is supported by the U.S. Department of Energy, Office of Science, Office of Basic Energy Sciences under Contract No. DE-AC02-76SF00515. Special thanks to J. Busan and the Northwestern University Research Machine Shop.

Received: ((will be filled in by the editorial staff))
Revised: ((will be filled in by the editorial staff))
Published online: ((will be filled in by the editorial staff))

References

[1] B. D. Paulsen, K. Tybrandt, E. Stavrinidou, J. Rivnay, *Nature Materials* **2020**, *19*, 13.
[2] J. Rivnay, R. M. Owens, G. G. Malliaras, *Chem. Mater.* **2014**, *26*, 679.
[3] S. Muench, A. Wild, C. Friebe, B. Häupler, T. Janoschka, U. S. Schubert, *Chem. Rev.* **2016**, *116*, 9438.
[4] P. M. Beaujuge, J. R. Reynolds, *Chem. Rev.* **2010**, *110*, 268.
[5] Y. van de Burgt, A. Melianas, S. T. Keene, G. Malliaras, A. Salleo, *Nature Electronics* **2018**, *1*, 386.
[6] L. Q. Flagg, R. Giridharagopal, J. Guo, D. S. Ginger, *Chem. Mater.* **2018**, *30*, 5380.
[7] C. Cendra, A. Giovannitti, A. Savva, V. Venkatraman, I. McCulloch, A. Salleo, S. Inal, J. Rivnay, *Advanced Functional Materials* **2019**, *29*, 1807034.
[8] C. G. Bischak, L. Q. Flagg, K. Yan, T. Rehman, D. W. Davies, R. J. Quezada, J. W. Onorato, C. K. Luscombe, Y. Diao, C.-Z. Li, D. S. Ginger, *arXiv:1910.06440 [cond-mat, physics:physics]* **2019**.

[9] R. Noriega, J. Rivnay, K. Vandewal, F. P. V. Koch, N. Stingelin, P. Smith, M. F. Toney, A. Salleo, *Nature Materials* **2013**, *12*, 1038.
[10] S. Fratini, M. Nikolka, A. Salleo, G. Schweicher, H. Sirringhaus, *Nature Materials* **2020**, *19*, 491.
[11] J. O. Guardado, A. Salleo, *Advanced Functional Materials* **2017**, *27*, DOI 10.1002/adfm.201701791.
[12] E. M. Thomas, M. A. Brady, H. Nakayama, B. C. Popere, R. A. Segalman, M. L. Chabinyc, *Advanced Functional Materials* **2018**, *28*, 1803687.
[13] J. L. Thelen, S.-L. Wu, A. E. Javier, V. Srinivasan, N. P. Balsara, S. N. Patel, *ACS Macro Lett.* **2015**, *4*, 1386.
[14] C. M. Palumbiny, F. Liu, T. P. Russell, A. Hexemer, C. Wang, P. Müller-Buschbaum, *Advanced Materials* **2015**, *27*, 3391.
[15] E. F. Manley, J. Strzalka, T. J. Fauvell, N. E. Jackson, M. J. Leonardi, N. D. Eastham, T. J. Marks, L. X. Chen, *Advanced Materials* **2017**, *29*, 1703933.
[16] H. Shi, C. Liu, Q. Jiang, J. Xu, *Advanced Electronic Materials* **2015**, *1*, 1500017.
[17] N. Kim, S. Kee, S. H. Lee, B. H. Lee, Y. H. Kahng, Y.-R. Jo, B.-J. Kim, K. Lee, *Advanced Materials* **2014**, *26*, 2268.
[18] S.-M. Kim, C.-H. Kim, Y. Kim, N. Kim, W.-J. Lee, E.-H. Lee, D. Kim, S. Park, K. Lee, J. Rivnay, M.-H. Yoon, *Nature Communications* **2018**, *9*, 3858.
[19] J. Rivnay, S. Inal, B. A. Collins, M. Sessolo, E. Stavrinidou, X. Strakosas, C. Tassone, D. M. Delongchamp, G. G. Malliaras, *Nature Communications* **2016**, *7*, 11287.
[20] Y. Honma, K. Itoh, H. Masunaga, A. Fujiwara, T. Nishizaki, S. Iguchi, T. Sasaki, *Advanced Electronic Materials* **2018**, *4*, 1700490.
[21] Y. W. Chen, J. D. Prange, S. Dühnen, Y. Park, M. Gunji, C. E. D. Chidsey, P. C. McIntyre, *Nature Materials* **2011**, *10*, 539.
[22] P. F. Satterthwaite, A. G. Scheuermann, P. K. Hurley, C. E. D. Chidsey, P. C. McIntyre, *ACS Appl. Mater. Interfaces* **2016**, *8*, 13140.
[23] C. Cao, I. I. Abate, E. Sivonxay, B. Shyam, C. Jia, B. Moritz, T. P. Devereaux, K. A. Persson, H.-G. Steinrück, M. F. Toney, *Joule* **2019**, *3*, 762.
[24] H.-G. Steinrück, C. Cao, G. M. Veith, M. F. Toney, *J. Chem. Phys.* **2020**, *152*, 084702.
[25] O. Bubnova, Z. U. Khan, A. Malti, S. Braun, M. Fahlman, M. Berggren, X. Crispin, *Nat Mater* **2011**, *10*, 429.
[26] N. Massonnet, A. Carella, O. Jaudouin, P. Rannou, G. Laval, C. Celle, J.-P. Simonato, *Journal of Materials Chemistry C* **2014**, *2*, 1278.
[27] S. Rudd, J. F. Franco-Gonzalez, S. K. Singh, Z. U. Khan, X. Crispin, J. W. Andreasen, I. Zozoulenko, D. Evans, *Journal of Polymer Science Part B: Polymer Physics* **2018**, *56*, 97.
[28] I. Zozoulenko, A. Singh, S. K. Singh, V. Gueskine, X. Crispin, M. Berggren, *ACS Appl. Polym. Mater.* **2019**, *1*, 83.
[29] A. V. Volkov, K. Wijeratne, E. Mitraka, U. Ail, D. Zhao, K. Tybrandt, J. W. Andreasen, M. Berggren, X. Crispin, I. V. Zozoulenko, *Advanced Functional Materials* **2017**, *27*, 1700329.
[30] K. Tybrandt, I. V. Zozoulenko, M. Berggren, *Science Advances* **2017**, *3*, eaao3659.
[31] A. Giovannitti, R. B. Rashid, Q. Thiburce, B. D. Paulsen, C. Cendra, K. Thorley, D. Moia, J. T. Mefford, D. Hanifi, D. Weiyuan, M. Moser, A. Salleo, J. Nelson, I. McCulloch, J. Rivnay, *Adv. Mater.* **2020**, 1908047.
[32] D.-M. Smilgies, *J Appl Cryst* **2009**, *42*, 1030.
[33] B. E. Warren, *X-Ray Diffraction*, Dover, New York, **1990**.
[34] A. Savva, S. Wustoni, S. Inal, *J. Mater. Chem. C* **2018**, *6*, 12023.
[35] J. E. Cochran, M. J. N. Junk, A. M. Glaudell, P. L. Miller, J. S. Cowart, M. F. Toney, C. J. Hawker, B. F. Chmelka, M. L. Chabinyc, *Macromolecules* **2014**, *47*, 6836.

[36] D. T. Duong, C. Wang, E. Antono, M. F. Toney, A. Salleo, *Organic Electronics* **2013**, *14*, 1330.
[37] G. D. Spyropoulos, J. N. Gelinas, D. Khodagholy, *Science Advances* **2019**, *5*, eaau7378.
[38] J. Rivnay, P. Leleux, M. Ferro, M. Sessolo, A. Williamson, D. A. Koutsouras, D. Khodagholy, M. Ramuz, X. Strakosas, R. M. Owens, C. Benar, J.-M. Badier, C. Bernard, G. G. Malliaras, *Science Advances* **2015**, *1*, e1400251.
[39] P. D'Angelo, S. L. Marasso, A. Verna, A. Ballesio, M. Parmeggiani, A. Sanginario, G. Tarabella, D. Demarchi, C. F. Pirri, M. Cocuzza, S. Iannotta, *Small* **2019**, *15*, 1902332.
[40] Z. Jiang, *Journal of Applied Crystallography* **2015**, *48*, 917.
[41] K. E. Aasmundtveit, E. J. Samuelsen, L. A. A. Pettersson, O. Inganäs, T. Johansson, R. Feidenhans'l, *Synthetic Metals* **1999**, *101*, 561.
[42] K. E. Aasmundtveit, E. J. Samuelsen, O. Inganäs, L. A. A. Pettersson, T. Johansson, S. Ferrer, *Synthetic Metals* **2000**, *113*, 93.
[43] E.-G. Kim, J.-L. Brédas, *J. Am. Chem. Soc.* **2008**, *130*, 16880.
[44] M. N. Gueye, A. Carella, N. Massonnet, E. Yvenou, S. Brenet, J. Faure-Vincent, S. Pouget, F. Rieutord, H. Okuno, A. Benayad, R. Demadrille, J.-P. Simonato, *Chem. Mater.* **2016**, *28*, 3462.

Time-resolved operando scattering captures the transient microstructural changes of an organic mixed ionic-electronic conductor in response to dynamic electrochemical potential. The timescales of structural changes related to doping and dedoping are not symmetrical. Combined with spectroelectrochemical measurements, this study reveals the close relationship between microstructure transients and polaron-bipolaron population kinetics.

Keyword: Organic mixed conductors

Bryan D. Paulsen, Ruiheng Wu, Christopher J. Takacs, Hans-Georg Steinrück, Joseph Strzalka, Qingteng Zhang, Michael F. Toney, Jonathan Rivnay *

Time-Resolved Structural Kinetics of an Organic Mixed Ionic Electronic Conductor

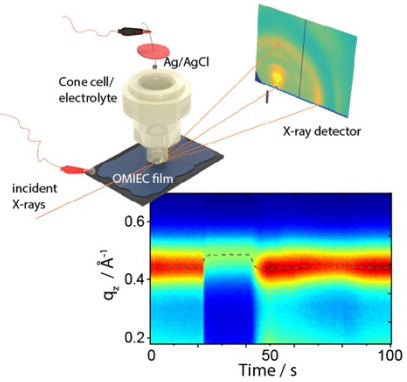

Copyright WILEY-VCH Verlag GmbH & Co. KGaA, 69469 Weinheim, Germany, 2018.

Supporting Information

Time-Resolved Structural Kinetics of an Organic Mixed Ionic Electronic Conductor

Bryan D. Paulsen, Ruiheng Wu, Christopher J. Takacs, Hans-Georg Steinrück, Joseph Strzalka, Qingteng Zhang, Michael F. Toney, Jonathan Rivnay

Experimental Section

Materials and Sample Preparation: PEDOT:PSS (Clevios PH-1000), purchased from Heraeus Holding GmbH, was filtered through 0.45 μm PES filters to remove large particles. For spectroelectrochemistry samples, the filtrate was spin-coated for 600 rpm for 60 s on pieces of 1 × 3 cm^2 ITO coated glasses (15-20 ohm sq^{-1}) (University Wafer) that prior to spinning had been successively sonicated in acetone and isopropyl alcohol, and cleaned with UV-ozone exposure. The cast films were dried on a hotplate in ambient at 120 ℃ for 10 minutes to remove water and then immersed into concentrated H_2SO_4 (Sigma-Aldrich, 95.0% - 98.0%) for 10 minutes at room temperature. After which the films were rinsed with DI water 3 times. and dried on a hotplate in ambient at 120 ℃ for 10 minutes. For the X-Ray scattering samples, the filtrate was drop-casted on a 1.5 x 3.5 cm^2 pieces of polished degenerately p-doped Si wafer (0.001-0.005 ohm cm^{-1}) (University Wafer) at 70 ℃ that prior to drop-casting had been successively sonicated in acetone and isopropyl alcohol, and cleaned with UV-ozone exposure. The drop-cast films were dried by the same method described above. Due to the thickness of the drop-cast film, the acid treat time was prolonged to 3 hours. After rinsing, the sample was first heated at 60 ℃ for 60 minutes and then 120 ℃ for 30 minutes on a hotplate in ambient. Resulting purple films were smooth and homogenous (under optical inspection), Figure S4.

Operando Visible-NIR Spectroscopy: Spectroelectrochemistry of acid crystallized PEDOT:PSS coated on ITO glass electrode was carried out in 100 mM aqueous NaCl in a PMMA cuvette with a Ag/AgCl pellet (Warner Instruments) reference/counter electrode. Potential control and current measurement was carried out with a potentiostat (Ivium). Simultaneous absorption spectroscopy was carried out with a halogen white light source (Ocean Optics, DH-2000-BAL) and an optical fiber light path split to separate UV-visible (Ocean Optics, FLAME-S) and near-infrared (Ocean Optics, NQ512) spectrometers, with 30 ms and 200 ms, resepctively. Electrochemical and spectroscopic data was recorded with Iviumsoft and OceanView software respectively. All analysis including curve merging, line cutting, and curve fitting were executed with MATLAB software.

Operando Grazing-Incidence Wide-Angle X-Ray Scattering: All time and voltage dependent GIWAXS measurements were performed at beamline 8-ID-E of the Advanced Photon Source, Argonne National Laboratory with 10.92 keV synchrotron radiation, 200 μm wide, focused to a 10 μm height, impinging on the sample with an incident angle of 0.14° (selected to be between the critical angle of the polymer and Si substrate, ~0.12° and 0.164° respectively), producing a 4 mm long beam foot print. The beam was vertically focused at the sample by a Be compound refractive lens composed of 17 lenslets with radius 0.2 mm positioned 2.175 m upstream of the sample The scattering was carried out under He atmosphere at room temperature with images collected by a Pilatus 1MF pixel array detector 228.2 mm away from the sample.

The operando cell was formed by pressing a machined knife edge polyether ether ketone (PEEK) cone against the PEDOT:PSS sample on a Si substrate supported by a polished quartz disk in a custom lens tube (Thorlabs) assembly. Electrochemical measurement and control employed the same potentiostat and reference/counter electrode employed in the above

described spectroelectrochemistry. The operando GIWAXS cells were sealed with a PTFE coated silicone septum. Films were cycled twice while exposed to the X-ray beam to assure the films were "broken in". For the CV and equilibrated step measurements, the integration time was set with 10 s to achieve a high signal to noise ratio. While the integration time for transient measurement was set to 0.5 s to capture structural transients. Good fits of the transient lamellar peaks required the combination of a Voigt peak with a varying center, width, and area, and a gaussian peak with varying width and area, but center fixed at q_z = 0.51 Å^{-1}, with an exponential fit of the background scattering, Figures S1, S5, and S6. The transient d_{100} values were calculated from the q_z value at the maximum intensity of the summation of these two fit peaks, which represented the average d_{100} at each given time step. All the GIWAXS data collected were processed with the GIXSGUI package for MATLAB.[40]

Static GIWAXS.

The 2-D scattering data (Figure S1) revealed a highly textured edge-on oriented structure, strong out-of-plane lamellar scattering *(h00)* and strong in-plane π-stack scattering *(0l0)*. In-plane (q_r) and out-of-plane (q_z) line cuts highlight the absence of lamellar ordering and the preponderance of π-stacking (020) in the plane of the film, and a strong lamellar scattering peak (100) and second order shoulder (200) out of the plane of the film. An in-plane peak at higher scattering vector (q_r ~ 2.5 Å^{-1}) is consistent with the PSS backbone scattering,[20] while the out-of-plane feature at (q_z ~ 1.35 Å^{-1}) appears to be a conflation of the PSS chain stacking[14] and the third order lamellar scattering. Some out-of-plane π-π stacking persists (q_z ~ 1.8 Å^{-1}), consistent with previous structural studies of acid crystalized PEDOT:PSS.[18] These data were consistent with the generally held crystal structure of lamellae of π-stacked PEDOT chains, separated by a layer of compensating anions (Tosylate or PSS chains).[14,17–20,41–44] The calculated π-stack and lamellar spacings of 3.54 Å and 13.3 Å, respectively, are in

good agreement with the d-spacings of PEDOT:PSS and in particular with the previous reports of acid crystallized PEDOT:PSS.

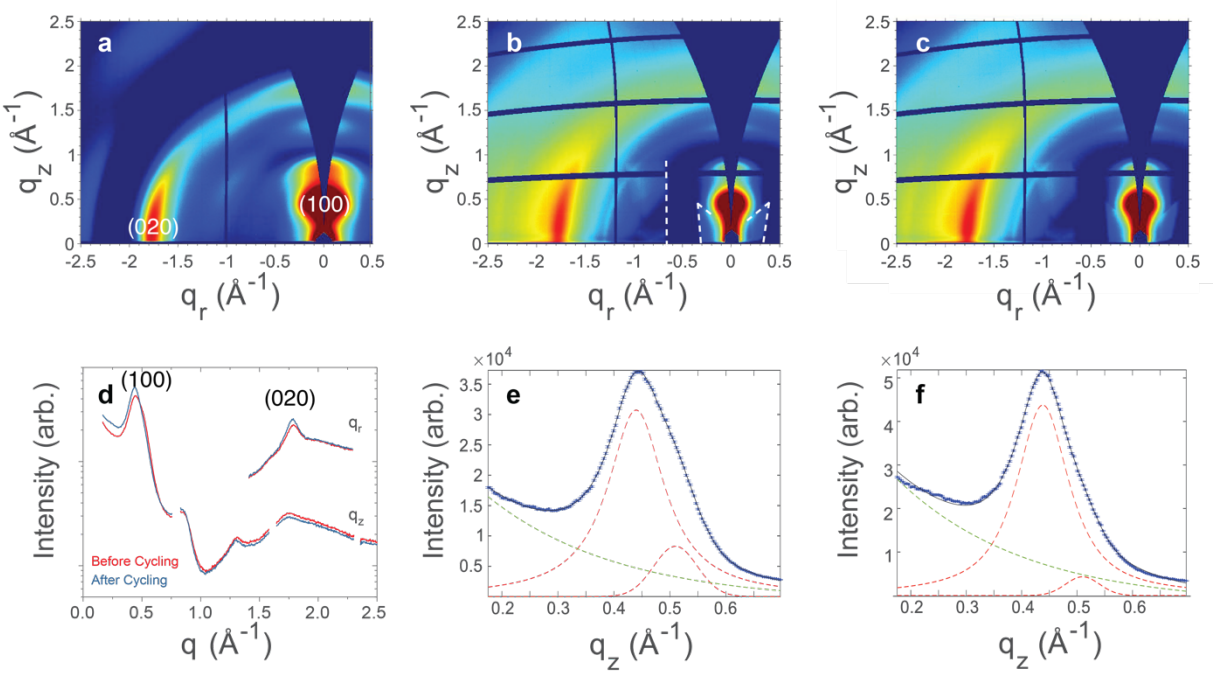

Figure S1. Static GIWAXS and long term stability: Two-dimensional grazing incidence X-ray q_r-q_z scattering map of acid crystallized PEDOT:PSS (a) as cast (stitched from images with different vertical detector position to fill vertical gaps between detector pixel array elements), and in the operando cone cell filled with aqueous 100 mM NaCl electrolyte (b) before and (c) after the completion of all cycling (~8 cycles, ~30 minutes of total beam exposure). Note in (b) and (c) that despite the increased diffuse (electrolyte) scattering at high q the out-of-plane lamellar and in-plane π-stack scattering is still evident. Dashed lines in (b) highlight the projected shadow of the operando cell and sample, discernible in areas of low scattering intensity, and arising from to upstream diffuse scattering due to a ~5 cm air gap separating the evacuated optics from the He purged sample chamber. (d) Nominally out-of-plane (q_z) and in-plane (q_r) line-cuts taken from 2-D scattering plots of PEDOT:PSS films in the operando cell before and after cycling. Two peak fitting of lamellar (100) peak for the film before cycling (e) and after long time cycling (f). Error bars in (e) and (f) are the instrumental error (i.e. square root of counts at given q vector).

Table S1. Long term stability: Fit peak centers and d-spacing at open circuit.

	$q_{Lamellar}$ (Å^{-1})	$d_{Lamellar}$ (Å)	$q_{\pi\pi Stacking}$ (Å^{-1})	$d_{\pi\pi Stacking}$ (Å)
Before	0.446	14.1	1.78	3.52
After initial cycling	0.441	14.2	1.78	3.52
After all measurements	0.439	14.3	1.78	3.52

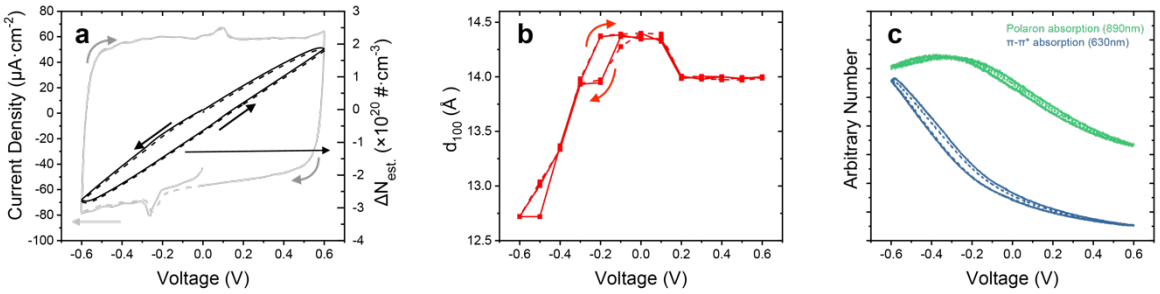

Figure S2. (a) Cyclic voltammogram (grey) during operando GIWAXS at a sweep rate of 5 mV/s with estimated modulated charge density (black) (referenced vs the charge density at 0.0 V vs Ag/AgCl). (b) Lamellar d-spacing and (c) neutral and polaron absorptions during cyclic voltammetry. Two cycles plotted of each with: first cycle solid lines, second cycle dashed lines. Note the d-spacing hysteresis in (b) between -0.2 and -0.3 V vs Ag/AgCl.

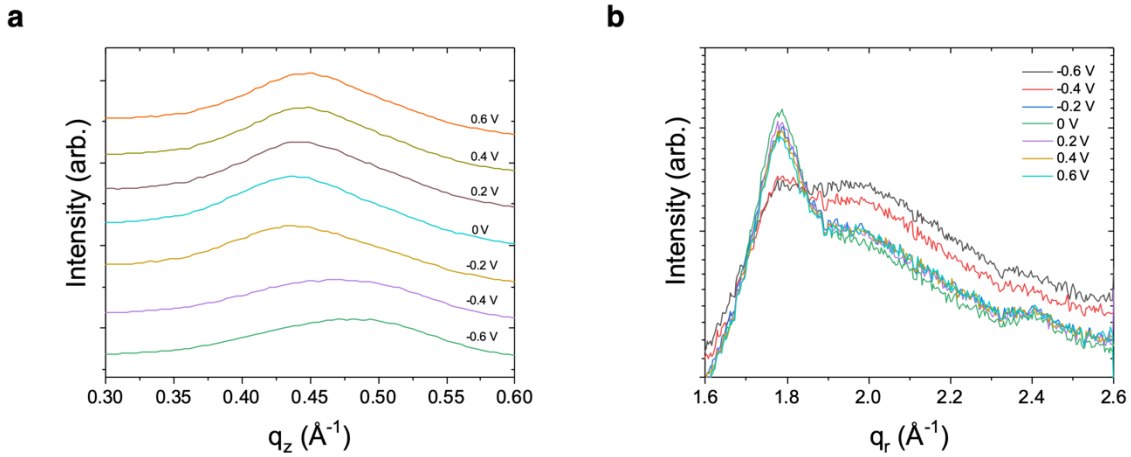

Figure S3. Line cuts of (a) out-of-plane lamellar and (b) in-plane π-stack scattering peaks collected from equilibrated fixed potential GIWAXS scattering plots. Line cuts in (a) have been offset to accentuate the peak shift.

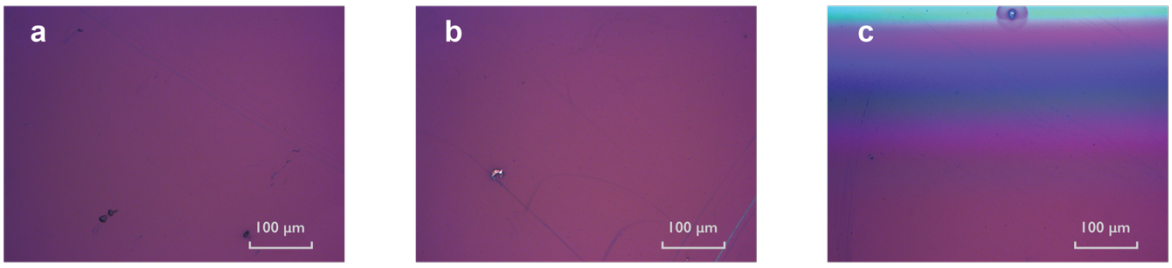

Figure S4. Representative 20× magnified optical microscope images of the drop-cast film (a) and (b) in the center of the substrate highlighting the largely continuous homogeneous surface of the film, and (c) of the film edge near the substrate edge where the thickness variation is visually apparent as color variation due to "coffee-ring" edge effects. Note, the operando cone cell was assembled on the center of the substrate where film homogeneity was best, and the remaining film outside the cone cell was removed manually.

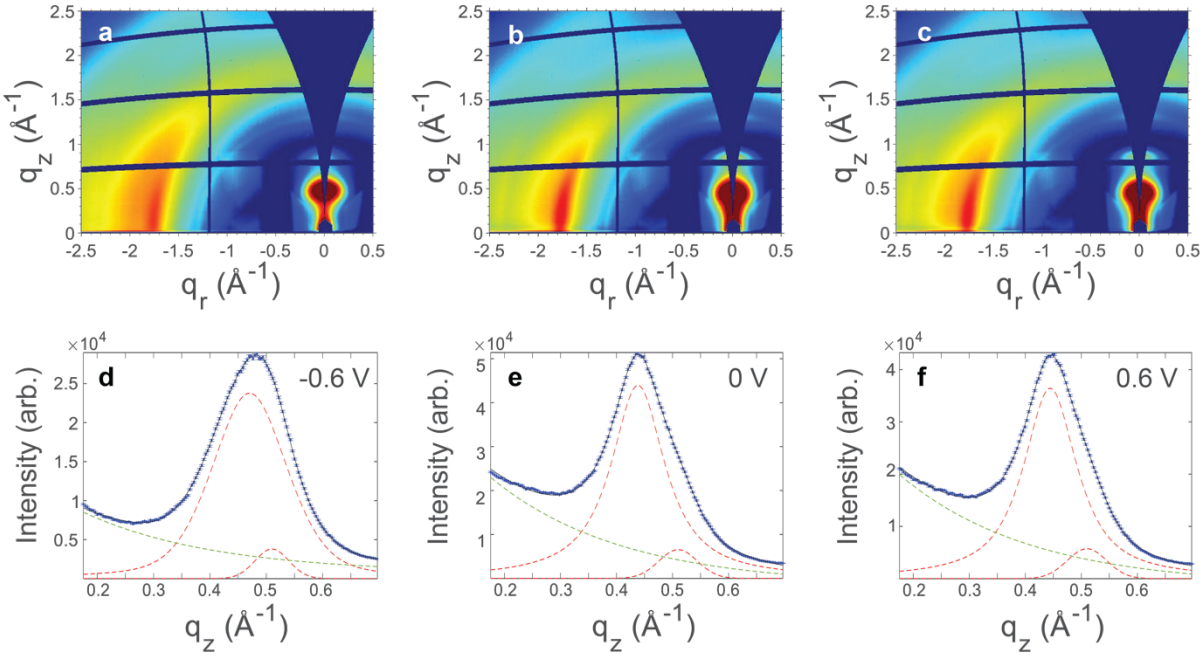

Figure S5. Representative two-dimensional grazing incidence X-ray q_r-q_z scattering maps of acid crystallized PEDOT:PSS during equilibrated 10 s exposures at (a) the lowest applied voltage (-0.6 V vs Ag/AgCl), (b) intermediate applied voltage (0 V vs Ag/AgCl), and (c)

highest applied voltage (+0.6 V vs Ag/AgCl). Respective fits of the out-of-plane lamellar (100) scattering at (d) -0.6, (e) 0, and (f) +0.6 V vs Ag/AgCl. Error bars in (d), (e), and (f) are the instrumental error (i.e. square root of counts at given q vector).

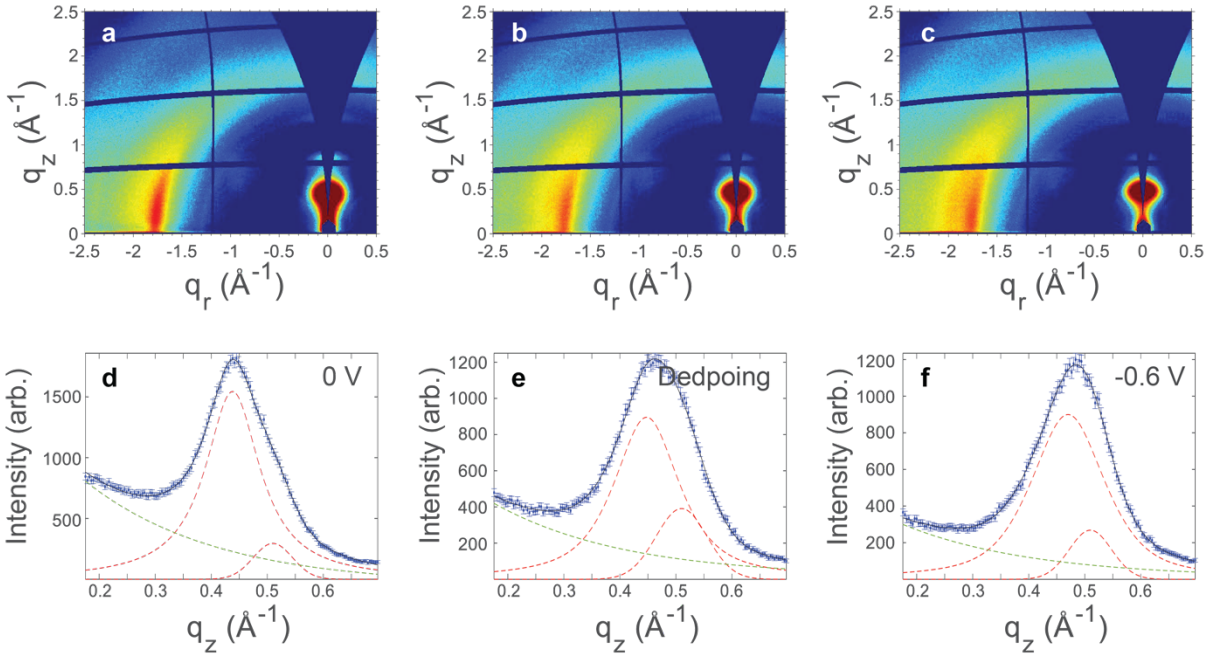

Figure S6. Representative two-dimensional grazing incidence X-ray q_r-q_z scattering maps of acid crystallized PEDOT:PSS during operando transient measurements from single 0.5 s exposure frames (a) before the voltage step (0 V vs Ag/AgCl), (b) in the midst rapid lamellar contraction during the dedoping immediately following the voltage step to -0.6 V vs Ag/AgCl, and (c) after equilibrating for some time at -0.6 V vs Ag/AgCl. Respective fits of the out-of-plane lamellar (100) scattering (d) before the voltage step, (e) in the midst rapid lamellar contraction immediately following the voltage step, and (f) after equilibrating after the voltage step. Error bars in (d), (e), and (f) are the instrumental error (i.e. square root of counts at given q vector).

Transient and Kinetic Model Fitting. Due to the large time step (0.5s) over which scattering was averaged, the d-spacing transient was fit empirically with an asymmetric sigmoidal function.

$$\boldsymbol{d(t) = \frac{d_f - d_i}{\left(1+exp\left(\frac{t-t_i}{\tau_d}\right)\right)^5} + d_i} \quad \text{(S1)}$$

The exponent was fixed large and positive, while the time constant (τ_d) and inflection point (t_i) were allowed to vary, and d_i and d_f were the initial and final lamellar d-spacings.

The normalized chronocoulometric transients were fit with a simple exponential function.

$$\boldsymbol{\frac{q(t)}{q_f} = -exp\left(\frac{-t}{\tau_q}\right) + 1} \quad \text{(S2)}$$

Where q_f is the final equilibrated charge and τ_q is the *RC* charging time constant.

The transients of the π-π* absorption (A_n) during dedoping (0 to -0.6 V vs Ag/AgCl) were fit as the final product of two consecutive elementary reactions.

$$\boldsymbol{A_n(t) = \left(A_{n,f} - A_{n,i}\right)\left(1 + \frac{k_{bp\to p}}{k_{p\to n} - k_{bp\to p}} exp\left(-k_{p\to n}t\right) - \frac{k_{p\to n}}{k_{p\to n} - k_{bp\to p}} exp\left(-k_{bp\to p}t\right)\right) + A_{n,i}} \quad \text{(S3)}$$

Where $A_{n,i}$ and $A_{n,f}$ were the initial and final π-π* absorption values, respectively, and $k_{bp\to p}$ and $k_{p\to n}$ were the bipolaron to polaron and polaron to neutral rate constants, respectively. For all other potential steps the π-π* absorption transients were fit as a single elementary reaction.

$$\boldsymbol{A_n(t) = (A_{n,i} - A_{n,f})exp(-k_x t) + A_{n,f}} \quad \text{(S4)}$$

Where k_x represented $k_{n\to p}$ and $k_{p\to n}$ depending of potential step. The transients of the polaron absorption (A_p) during doping and dedoping between 0 and -0.6 V vs Ag/AgCl were fit as the intermediary of two consecutive elementary reactions. During doping taking the form:

$$\boldsymbol{A_p(t) = N\left(\frac{k_{n\to p}}{k_{p\to bp} - k_{n\to p}}\left((1+\alpha)exp\left(-k_{n\to p}t\right) - (1-\alpha)exp\left(-k_{p\to bp}t\right)\right)\right) + A_{p,f}} \quad \text{(S5)}$$

And during dedoping taking the form:

$$\boldsymbol{A_p(t) = BP\left(\frac{k_{bp\rightarrow p}}{k_{p\rightarrow n}-k_{bp\rightarrow p}}\left((1+\alpha)exp(-k_{bp\rightarrow p}t) - (1-\alpha)exp(-k_{p\rightarrow n}t)\right)\right) + A_{p,f}} \quad \text{(S6)}$$

Where α was an empirical fit parameter, and N and BP are constants proportional to the initial neutral and bipolaron populations, respectively; and $k_{n\rightarrow p}$, $k_{p\rightarrow bp}$, $k_{bp\rightarrow p}$, and $k_{p\rightarrow n}$ were the neutral to polaron, polaron to biopolar, bipolaron to polaron, and polaron to neutral rate constants, respectively. For all other potential steps the polaron absorption transients were fit as a single elementary reaction.

$$\boldsymbol{A_p(t) = (A_{p,i} - A_{p,f})exp(-k_x t) + A_{p,f}} \quad \text{(S7)}$$

Where k_x represented $k_{p\rightarrow n}$ and $k_{p\rightarrow bp}$ depending of potential step, and $A_{p,i}$ was the initial polaron absorption value.